Journal of the European Ceramic Society 43 (2023) 5894–5903

Contents lists available at ScienceDirect

Journal of the European Ceramic Society

journal homepage: www.elsevier.com/locate/jeurceramsoc

Laser surface texturing and numerical simulation of heat flux on Cr_2AlC MAX phase heat exchangers

J. Mesquita-Guimarães [a,b,*], N.M. Ferreira [c], R.M.S. Reis [a,b], J. Gonzalez-Julian [d,e], J. Pinho-da-Cruz [a,b]

[a] TEMA – Centre for Mechanical Technology and Automation, Department of Mechanical Engineering, University of Aveiro, 3810-193 Aveiro, Portugal
[b] LASI - Intelligent Systems Associate Laboratory, Portugal
[c] i3N – Institute for Nanostructures, Nanomodelling and Nanofabrication, Department of Physics, University of Aveiro, 3810-193 Aveiro, Portugal
[d] Institute of Mineral Engineering, Department of Ceramics, RWTH Aachen University, 52074 Aachen, Germany
[e] Institute of Energy and Climate Research, Materials Synthesis and Processing (IEK-1), Forschungszentrum Jülich GmbH, 52425 Jülich, Germany

ARTICLE INFO

Keywords:
MAX phase
Cr_2AlC
Plate heat exchanger
Microchannels
Laser surface texturing
Concentrated solar power
Thermal analysis
Heat flux

ABSTRACT

The energetic worldwide emergency demands a significant drop in fossil energy to renewable energies as part of the sustainable solutions for global energy consumption. MAX phase materials, such as Cr_2AlC, are potential candidates for heat exchanger applications due to their excellent oxidation and corrosion resistance, good thermal shock response and relatively high thermal conductivity. This study uses laser surface texturing (LST) technology to design plate heat exchanger patterns on the Cr_2AlC MAX phase. Furthermore, performing numerical simulations on textured plate models under molten salt conduction and convection conditions, accessing temperature gradient and heat transfer behaviour were conducted on Cr_2AlC, as well as on 316 L stainless steel and alumina for comparison. As a result, combined microtextures with a corrugated surface and spaced V-shape channels were obtained using LST in a single step. The parametric study indicated that the optimal channels (groves) were found for 25 W in air and 20 s laser conditions, with approximately 145 μm width and 340 μm depth. Furthermore, the numerical simulation showed that ceramics materials present better heat transfer conditions than 316 L stainless steel, where Cr_2AlC and alumina only differ in 1.9% heat flux. In addition, the corrugated surface plate with 2.6% width of the total thickness increases heat transfer by 9.8%.

1. Introduction

Over the years, the efficiency of energy systems has been improved by resorting to new materials, new technologies, and system simulation. In line with the great demand to drop fossil energies and move to renewable energies, there are higher requirements to improve the efficiency of energy systems of natural resources [1,2]. Likewise, materials such as phase change materials (PCMs) [3], lithium and nickel alloys [4], and 2D and layered oxide-based zeolites and perovskites [5] have gained interest in several energetic technologies, such as production, harvesting or storage energy systems, to guarantee excellent efficiency. In addition, different equipment types can be found as component systems, such as collectors, boilers, heat exchangers, turbines, tanks, etc. [6]. In particular, heat exchangers are devices that allow heat transfer between two fluids at different temperatures separated by a flux passage [7]. Focus on solar energy, the second renewable technology worldwide after wind, photovoltaic and solar panels are now competing with new solar power technology being implemented worldwide called concentrated solar power (CSP) plants [8,9]. In CSP systems, the heat transfer fluids (HFT) should be more stable at high temperatures than others, such as silicon oil or water, having maximum temperature uses until 360 °C [10,11]. Here, in the solar receivers, the heat is concentrated by the sunlight and transferred to the heat transfer fluid, like molten salts, reaching temperatures higher than 550 °C [10,11]. The molten salts for CSP resist high temperatures and are environmentally friendly due to their high thermal capacity, low melting point, high boiling point and low viscosity [12,13]. The choice of resistant heat exchanger materials is essential for such aggressive conditions. Initially, heat exchangers were produced using metallic alloys due to the feasibility of manufacturing complex shapes; however, they are not ideal when facing aggressive

* Corresponding author at: TEMA – Centre for Mechanical Technology and Automation, Department of Mechanical Engineering, University of Aveiro, 3810-193 Aveiro, Portugal.
E-mail address: joanaguimaraes@ua.pt (J. Mesquita-Guimarães).

https://doi.org/10.1016/j.jeurceramsoc.2023.06.031
Received 7 March 2023; Received in revised form 9 June 2023; Accepted 12 June 2023
Available online 13 June 2023

conditions, such as corrosion and tribological and mechanical capabilities that degrade at high temperatures. Based on that, other materials, such as refractory ceramics like SiC [14,15], and ZrC [16], began to be studied as potential substitutes. The two significant advantages of using ceramics and ceramic matrix composites are their mechanical integrity and high-temperature corrosion resistance, potentially increasing the components' lifetime. However, their manufacture can be challenging when compared to metallic alloys.

A new family of materials, called MAX Phases, has grown exponentially during the past few years. MAX Phases are nano-layered ternary carbides and nitrates compounds with the general formula of $M_{n+1}AX_n$, M a transition metal, A an element of group A of the periodic table and X an atom of nitrogen or carbon [17]. It is a very particular material since it combines metal and ceramic properties, such as low density, low hardness, good machinability, high strength and high Young's modulus at high temperature, high chemical resistance, excellent thermal shock resistance, as well as high thermal and electrical conductivities [18,19]. The combination of the properties makes MAX phases highly attractive as potential structural materials for high-temperature applications [17].

Easily high thermal conductivity materials are related to high thermal efficiency. The thermal conductivity of the most used materials on plate heat exchangers ranges between metallic alloys, such as stainless steel and nickel alloys, which vary from 17 W/(m·K) [20] to 28 W/(m·K) [14], respectively. On ceramics materials, the range can be wider, presenting 90 W/(m·K) for SiC and 29 W/(m·K) for Al_2O_3 [15]. In MAX phase family materials, Ti_2AlC has a thermal conductivity of 32 W/(m·K) [21] and Cr_2AlC of 22 W/(m·K) [17].

Heat exchangers present several configurations: shell and tube, bitubular, spiral, air-cooled and plate [22]. Regarding the topography of the heat exchanger plates, several patterns can be found in the literature: Chevron or herringbone (fishbone), washboard (washing board), zigzag, and protrusions and depressions (corrugate) [23]. The conventional production procedures for obtaining such topographies on ceramic heat exchangers are often complex, such as low-temperature cofired ceramics (LTCC) and the extrusion-free forming (EFF) method with multi-steps to achieve microchannels [24,25].

In the last decades, laser technology has been widely used in machining techniques for writing, cutting, texturing, welding and sintering [26]. The high-energy laser beam interacts with the surface material, sublimising and causing a small surface area ablation. Laser surface texturing (LST) is becoming increasingly popular as one of the most practical micro-texturing solutions, such as microchannel patterning [26]. To the author's knowledge, there is no reference to laser beam interaction with the Cr_2AlC MAX phase to achieve material ablation.

In this work, a solid-state laser was used, the Neodymium doped Yttrium Aluminum Garnet (Nd:YAG), to promote ablation in the MAX phase surface material and perform surface texturisation. LST is a powerful method to texturise complex surface geometries with high resolution and precision compared to other texturing technologies optimising power laser, frequency, speed and time exposure [27,28]. In addition, it is a process with a high-speed texturing step, allowing a decrease in process time, providing excellent control of the shape and size of the channels, making easy creation of optimal designs, and is environmentally friendly [28].

A numerical analysis based on the Finite Element Method (FEM) was used to analyse the heat exchangers' efficiency regarding the plate's maximum temperature and heat flux when a channel dimension's variation is created via laser surface texturing [29,30].

The main objective of this study was to find the optimised geometry channel for a microplate heat exchanger using the Cr_2AlC MAX phase as material and using a texturing technology by laser ablation. In order to reach this goal, it was necessary to test the plate's temperature and heat flux behaviour when the width and depth of the channel vary. For that, a parametric analysis using simulation software can easily predict the performance of the channels. Therefore, in this study was possible to; i) determine the thermal properties of the Cr_2AlC MAX phase using the measured properties by adding them to the Solidworks database; ii) explore the possibilities of laser texturing through a matrix of conditions, varying mainly current and exposure time; iii) simulate textures' effect regarding temperature gradient and the heat flux across the plate; iv) perform a parametric study by varying the width and depth of the channels and mapping the laser microtextures; v) compare temperature gradient and heat flux of Cr_2AlC MAX Phase with the other reference materials, 316 L stainless steel and alumina, with and without corrugation.

2. Experimental procedure

2.1. Cr_2AlC max phase synthesis and samples preparation

Cr_2AlC samples were produced by reactive sintering (synthesis and sintering in the same thermal treatment) using chromium (Alfa Aesar, purity: 99%, d50: 28.0 μm), aluminium (Alfa Aesar, purity: 99.5%, D50 = 9.1 μm) and graphite (Alfa Aesar, purity: 99.0%, D50 = 6.9 μm) powders. The powders with a molar ratio of $Cr_2Al_{1.02}C_{0.97}$ were mixed in a roller bench for 24 h in ethanol using 5 mm diameter ZrO_2 milling balls and a power/ball ratio of 1:1. After the mixing step, the mixture was dried in a rotary evaporator and at 80 °C overnight in an oven. The reactive sintering was performed using Field Assisted Sintering Technology/Spark Plasma Sintering (FAST/SPS, FCT-HPD5, FCT Systeme GmbH, Germany). The sintering conditions were: a heating rate of 50 K/min, a maximal temperature of 1250 °C, uniaxial pressure of 30 MPa, a dwell time of 20 min and a vacuum (~4 mbar) during the whole thermal cycle. The temperature was controlled using a pyrometer focused on the surface of a drilled punch at only 5 mm from the powder. The sintered Cr_2AlC samples were ground and polished to eliminate the remaining graphite and prepare the surface for laser texturing.

2.2. Laser texturing procedure and technical analysis

The texturing step was performed accessing Q-switched Nd:YAG laser (StarMark SMP 100II Rofin-Basel, Germany) emitting up to 50 W at 1064 nm with a fixed pulse duration of 100 ns coupled to a galvanometric head. The total spacial control of the beam laser, through a scan head, allow employed a mobile table from Thorlab (MTS 50/M-Z8), and the sample speed was kept constant for 5 mm/s in a single direction. An additional stopping step in the sample motion at every 500 μm with an exposition time (10 or 20 s) was performed to design a complex texture surface. In addition, a gas extraction/filtering system was also accomplished.

The surface and cross-section analysis of the laser texturing patterns was performed by accessing a scanning electronic microscope TM4000Plus (Hitachi, Japan) and for the dimensional characterisation of the pattern accessing the measuring tool. For the topographic analysis of the microtextured surfaces, an optical profilometer S-Neox (Sensofar, Spain) and SensoScan 6.2 software were used. Depending on surface depth analysis, the measurements were carried out using the confocal and vertical shift interferometry mode. The analysis has run using the lens of 10x to 50x. Sensomap software to extract surface profiles was used. Furthermore, the CAD design of the combined microtexture was created by composing the size information collected from 3D profilometer measurements (limited $\geq$ 100 μm) with the precise groove width and depth measurements obtained from SEM micrographs, as demonstrated in the following sections.

2.3. Numerical simulation procedure

2.3.1. Thermal considerations

The temperature and heat flux gradient of Cr_2AlC (MAX phase) was determined via numerical simulation and compared with other reference materials for heat exchangers application, in particular 316 L

Table 1
Thermomechanical properties of the materials used in this study. 316 L stainless steel properties were already on the Solidworks database. The Cr_2AlC properties were compiled from the experimental results of this work and literature [34]; alumina properties from the literature [15].

Properties	316 L Stainless Steel	Cr_2AlC	Alumina
Young's modulus [GPa]	200	250	340
Poisson's ratio [-]	0.27	0.20	0.20
Mass density [g/cm^3]	8.00	5.15	3.90
Thermal Conductivity [W/(m·K)]	14.60	22.97	29.00
Thermal expansion coefficient [K^{-1}]	16.5×10^{-6}	12.3×10^{-6}	7.5×10^{-6}
Specific heat [J/(kg·K)]	450	650	850

Table 2
Molten salt thermal properties at 300 °C [37].

Molten salt (60% $NaNO_3$-40% KNO_3)		
Stable Operating Temperature [ºC]	$T_{op,fluid}$	550
Thermal Mass Capacity [J/(kg·ºC)]	cp_{fluid}	1492
Thermal Conductivity [W/(m·ºC)]	k_{fluid}	0.498
Viscosity [Pa.s]	μ_{fluid}	3.56×10^{-3}

Table 3
Reynolds, Prandtl and Nusselt numbers used to calculate the convection heat transfer coefficient value, h.

Reynolds number [-]	1000.00
Prandtl number [-]	10.66
Nusselt number [-]	46.21
Convection heat transfer coefficient, h [W/(m^2·K)]	1841.07

stainless steel (metal) and alumina (ceramic). Solidworks 2020 software was used to draw the CAD model and perform the thermal analysis. The thermal analysis was performed considering conduction and convection mechanisms. Conduction refers to heat transfer within the body, and convection refers to heat transfer between the body and the surrounding environment [22].

2.3.2. Plate model and materials thermomechanical properties

The simulation analysis was performed considering ceramic microplate heat exchanger dimensions of 1 mm thickness, 12.5 mm length and 7.5 mm width [31–33]. The following Table 1 presents the thermomechanical properties of the studied materials 316 L stainless steel (metal), Cr_2AlC (MAX phase) and alumina (ceramic) used in the simulation software.

Mass density, thermal conductivity and thermal expansion coefficient were determined experimentally. Mass density was determined via the Archimedes method, and the obtained relative density of 98.3 ±0.4% is associated with highly dense material, similarly shown by Gonzalez-Julian et al. [35]. The thermal expansion coefficient was measured via dilatometry, which measures thermal expansion as a function of temperature. Measurements were performed on a BAHR Dil801L - Furnace 7040 (BAHR - Thermoanalyse GmbH, Germany). The thermal cycle was up to 1400 °C with a heating rate of 10 °C/min. The thermal expansion coefficient was obtained by fitting the dilatometric curve in the range from 200 ºC to 1200 °C, obtaining 12.3×10^{-6}°C^{-1}, following the reported literature [34].

Thermal conductivity was measured using the hot disk transient flat source TPS method accessing the TPS 2500 S (hot disk instruments, Sweden). These measurements were performed with a Kapton 102003 sensor (r = 0.888 mm) and an electrical power of 35 mW, for 3 s, at an ambient temperature of 22.78 °C. The software allows the selection of the most accurate values from a group of 20 fitted values. The thermal conductivity result was obtained from the average of 5 measurements. The obtained result was 22.97 ± 0.60 W/(m·K), which is similar to the reported in the literature of 22 W/(m·K) [34]. Since both values are consistent with the literature, they can be used in the Solidworks database to describe the Cr_2AlC MAX phase material.

2.3.3. Heat fluid transfer analytic conditions

This study analyses the behaviour of a fluid passing through a plate, with and without channels. The heat transfer fluids generally used in concentrated solar power plants are oils, water/steam, air and molten salts [10,11,36]. The most common molten salts used on high-standard metallic materials, such as 316 L stainless steel and ferritic steel 91, are based on nitrates, such as $60\%NaNO_3 - 40\%KNO_3$, which has an operating temperature of up to 550 °C, high efficiency, and is cheaper and more environmentally friendly than oils [36,37]. The simulation study considered a fluid temperature of 550 ºC and a bottom surface temperature of 25 ºC, defining a film temperature of 287.5 ºC. In this context, the properties of this molten salt, such as thermal mass capacity cp_{fluid}, thermal conductivity k_{fluid}, and viscosity μ_{fluid}, were obtained from the literature for a temperature of 300 °C [37], as shown in Table 2.

Thus, convection will be considered between fluid and plate, and conduction through the thickness of the plate [38].

2.3.4. Initial and boundary conditions of the study

This section will set the initial and boundary conditions for the finite element method problem. Since surface geometry and fluid's thermal properties have already been calculated, it is fundamental to determine the nature of the fluid flux, which refers to a laminar or turbulent regime distinguished by the Reynolds number (Re). Unfortunately, the fluid input velocity is unknown in this work, which makes the Reynolds calculation unfeasible. Nevertheless, following the literature, it is possible to state that micro exchangers present Reynolds values between 500 and 1000, making this regime laminar [39]. Therefore, to simulate the most critical condition, Reynolds number (Re) was assumed as 1000. In order to determine the convection heat transfer coefficient, the Nusselt number (Nu) and Prandtl number (Pr), defined respectively by

$$\mathrm{Nu} = 0.664 \cdot \mathrm{Re}^{1/2} \cdot \mathrm{Pr}^{1/3}, \mathrm{Pr} \geq 0.6 \quad (1)$$

and

$$\mathrm{Pr} = \frac{cp_{fluid} \cdot \mu_{fluid}}{k_{fluid}} \quad (2)$$

were computed, where cp_{fluid} is the thermal mass capacity, μ_{fluid} the viscosity and k_{fluid} the thermal conductivity of the fluid. In this context, the heat transfer coefficient for the convection transfer process corresponds to [22].

$$h = \frac{\mathrm{Nu} \cdot k_{fluid}}{L_{plate}} \quad (3)$$

where L_{plate} is the length of the plate (12.5 mm). The values obtained from the equations presented above are shown in Table 3.

After creating the CAD model of the plate in SolidWorks, a "SolidWorks Thermal Analysis" was performed. In resume, the initial and boundary conditions considered for the thermal analyses in the plate are the following ones:

- Bottom surface plate condition: room temperature (25 °C) before the fluid's passage;.
- Top surface plate condition: Convection heat transfer coefficient between the plate and the fluid: h = 1841.1 W/(m^2·K)at T = 550 °C;.

Table 4
Nd:YAG laser tested conditions, such as scanning rate, frequency, atmosphere, power laser and exposition time.

Scanning rate [mm/s]	Frequency [kHz]	Atmosphere	Power laser [W]	Exposition time [s]
1000	20	air	22.5	10
				20
			25	10
				20
		argon	25	10
				20

- Sidewalls condition: Sidewalls of the plate are considered adiabatic (due to the symmetry of the problem): Heat flux is equal to 0 W/m^2..

3. Experimental results

3.1. Laser surface texturing characterisation

Three different parameters, the atmospheric conditions, power laser and exposition time, were studied, as shown in Table 4.

Table 4 shows that scanning rate and frequency were fixed parameters, 1000 (mm/s) and 20 (kHz), respectively. For the laser texturing optimisation, a matrix condition was used by varying the power laser between 20–25 W and the exposition time between 10 s and 20 s, under air and argon, resulting in 6 groups with 3 grooves per condition.

The total spatial control of the laser beam, through a scanning head used in the laser surface texturing process, allows the combination of micro-textures, such as a corrugated surface with a spaced V-shaped channel (groves), as shown in the following results.

In order to inspect the microtextures, SEM analyses were accessed. Also, the measurement tool was used to obtain a precise dimension of depth and width of the V-shaped channels, as illustrated in Fig. 1.

Fig. 1 shows the microtextured surfaces with two combined textures of a corrugated surface on a V-shape-spaced channel patterning. The authors would like to remark on the discovery of this laser texturing process that allows combining two levels of micro-texturing, maintaining constant laser conditions, only using sample motion.

Table 5
Average and standard deviation values for width and depth measurements of the V-shaped channels after the six texturing conditions.

Laser conditions	Width [μm]		Depth [μm]	
	10 s	20 s	10 s	20 s
22.5 W; air	137 ±3	138±7	271±7	332±29
25 W; air	153±6	144±5	294±18	338±16
25 W; argon	174±7	171±14	279±7	346±6

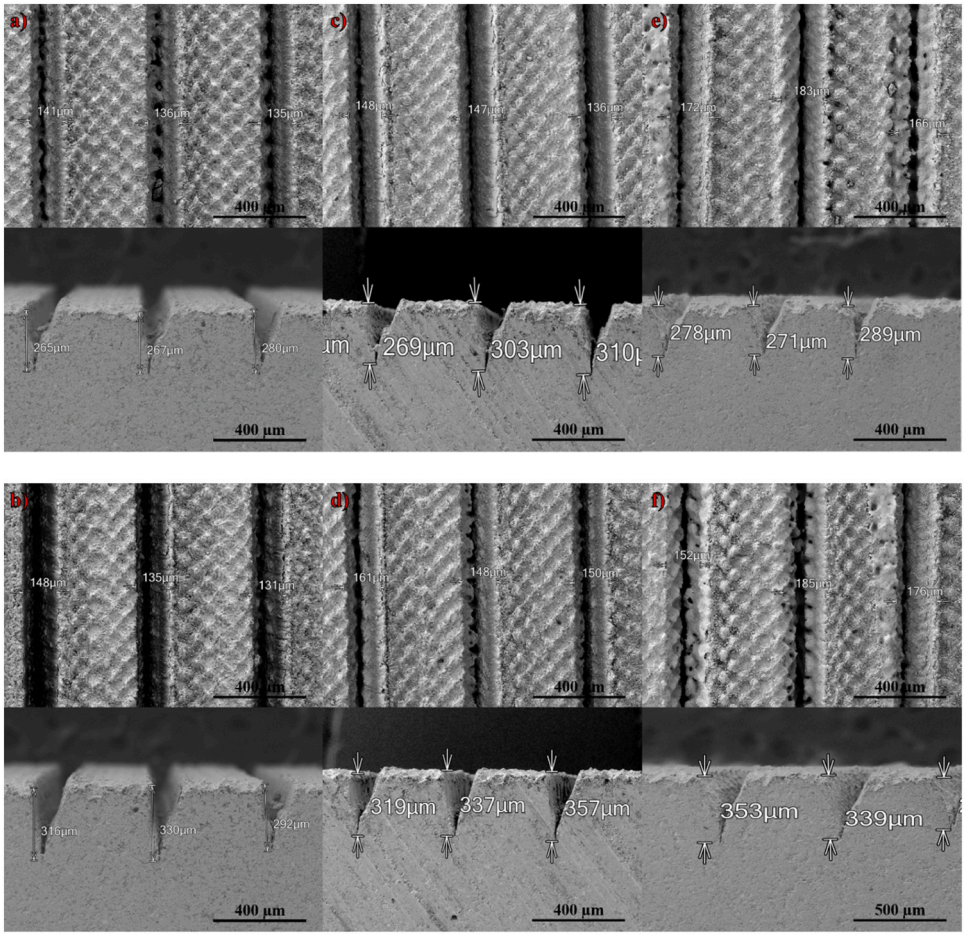

Fig. 1 –. SEM micrographs of microtextured channels, top view and cross-section: (a) 22.5 W for 10 s at air; (b) 22.5 W for 20 s at air; (c) 25 W for 10 s at air; (d) 25 W for 20 s at air; (e) 25 W for 10 s at argon; (d) 25 W for 20 s at argon.

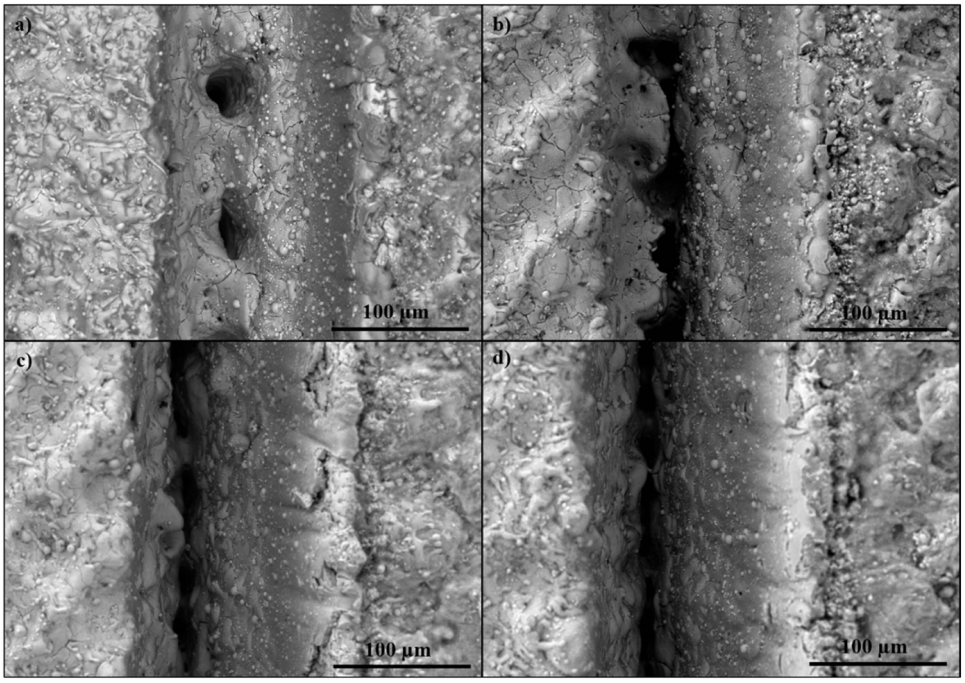

Fig. 2 –. Detailed view of V-shape channels to select cleaning parameters: (a) 22.5 W for 10 s at air; (b) 25 W for 10 s at air; (c) 22.5 W for 20 s at air; (d) 25 W for 20 s at air.

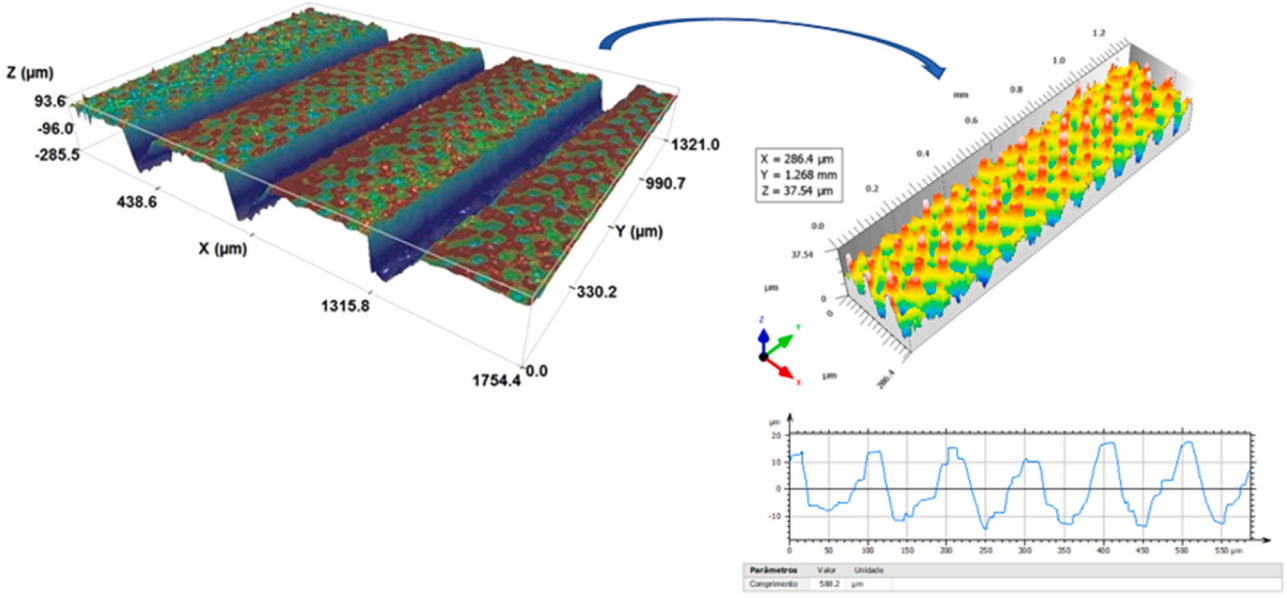

Fig. 3. - 3D surface and profile of the corrugated section of the combined texture (25 W; 20 s) using the lens of 10x and confocal mode.

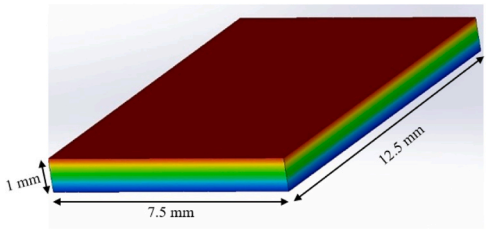

Fig. 4. - Solidworks simulation of temperature variation through the thickness plate.

Table 6
Analytical and numerical results for maximum wet temperature for the 316 L SS, Cr_2ALC and alumina plates.

Maximum wet temperature on the plate (T_{wet})		
Material	Analytical values [ºC]	Numerical values [ºC]
316 L Stainless steel	83.80	83.77
Cr_2AlC	63.95	63.95
Alumina	56.34	56.33

Table 7
Convergence study results to find the admissible mesh.

Element size [mm]	0.2	0.15	**0.1**	0.07	0.05
Tolerance [mm]	0.01	0.0075	**0.005**	0.0035	0.0025
Number of nodes & degrees of freedom	22685	57139	**168632**	435976	1053396
Number of elements	14397	38022	**115857**	305727	748711
Maximum temperature [°C]	76.27	76.20	**76.19**	76.19	76.19

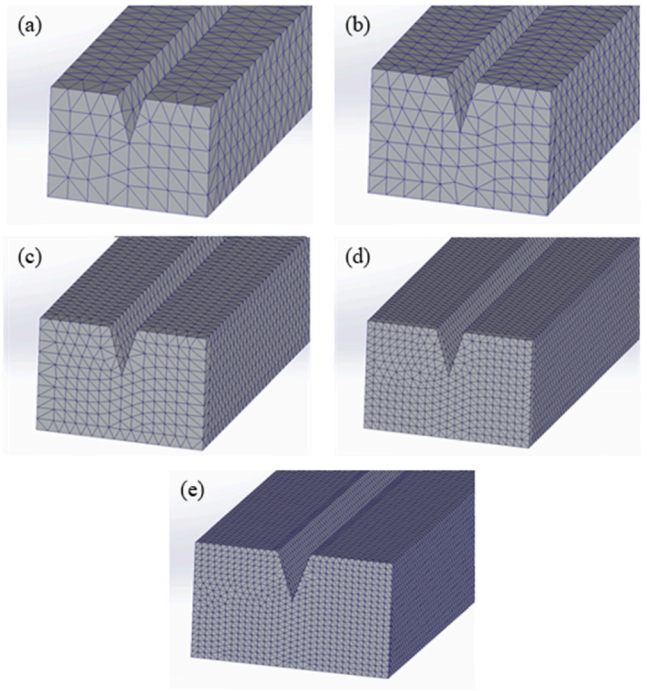

Fig. 5. - Meshes considered in the convergence study with element sizes of (a) 0.2 mm; (b) 0.15 mm; (c) 0.1 mm; (d) 0.07 mm; (e) 0.005 mm.

As mentioned before, the depth and width of the channels were measured by SEM, thus offering a more expeditious way to obtain precise measurements than a 3D profilometer, which has depth limitations at 300 μm depth. Table 5 shows the average and standard deviation values for the width and depth of the channels under the studied parameters.

The values remark the differences between width and depth, measured for each laser parameter. As expected, the results show the tendency for wider and deeper channels with increased power laser and exposure time [27]. For example, it is possible to observe that the average width value for 10 s and 20 s increases by approx. ~20 μm when the power laser increases, from 22.5 W to 25 W, at air and under argon. Likewise, depth values increase when exposure time increases from 10 s to 20 s, approx. ~55 μm. Fig. 2 shows the differences in V-shape channels by varying power laser and exposition time for a more defined and clean channel.

Fig. 2 shows the differences between the channels' depth, comparing the exposure time of 10–20 s for 22.5 W and 25 W power lasers. Notably, the V-shape channels get more defined and cleaner, with a smoother surface for longer exposition time and higher power laser. In summary, texturisation with 10 s at air can be excluded due to the lack of channel definition and smoothness. Therefore, inside the tested parameters, the best conditions for laser texturing are 25 W for power laser and 20 s exposition time at air, using 20 kHz frequency and 1000 mm/s for scanning rate.

For the topographic analysis of the combined surface textures, an optical profilometer was used to extract the depth measurement of the corrugated and V-shape channels and confirm the profile and measurements performed via SEM. Both confocal and vertical shift interferometry modes were used because confocal has a depth limitation of 100 μm, and interferometer mode could access the V-shape channels of 300 μm groves depth. Fig. 3 shows a 3D image of the combined microtextured surface, grooves and corrugated surface, using the lens of 10x and confocal mode.

The 3D profilometry analysis allowed for obtaining an accurate 3D surface and extracting the corrugated surface in detail. Fig. 3 shows the combined texture of corrugated surfaces and V-shape-spaced channels. In detail, the extracted corrugated section has a maximum height of ~40 μm (z_{max}), which corresponds to the distance between the highest peak and deepest valley, and the angle from peaks and valleys is 60°. The distance between the top of the peaks is ~100 μm, and their diameter is ~20 μm. The corrugated part corresponds to 2.6% of the total plate

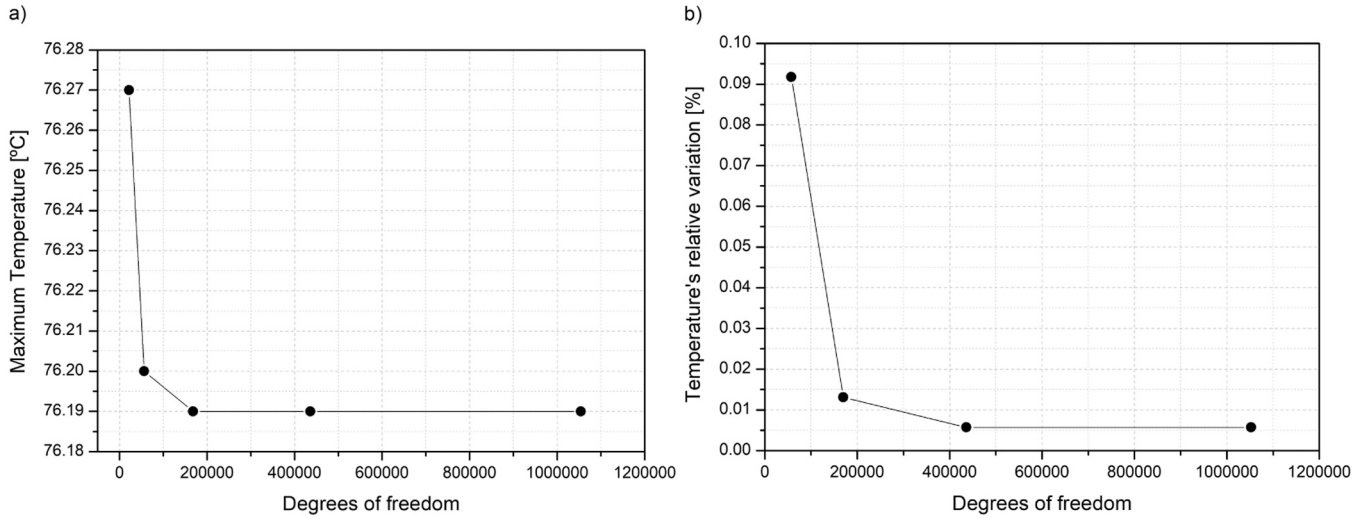

Fig. 6. - Evolution of (a) the maximum temperature; (b) the temperature's relative variation with the number of degrees of freedom.

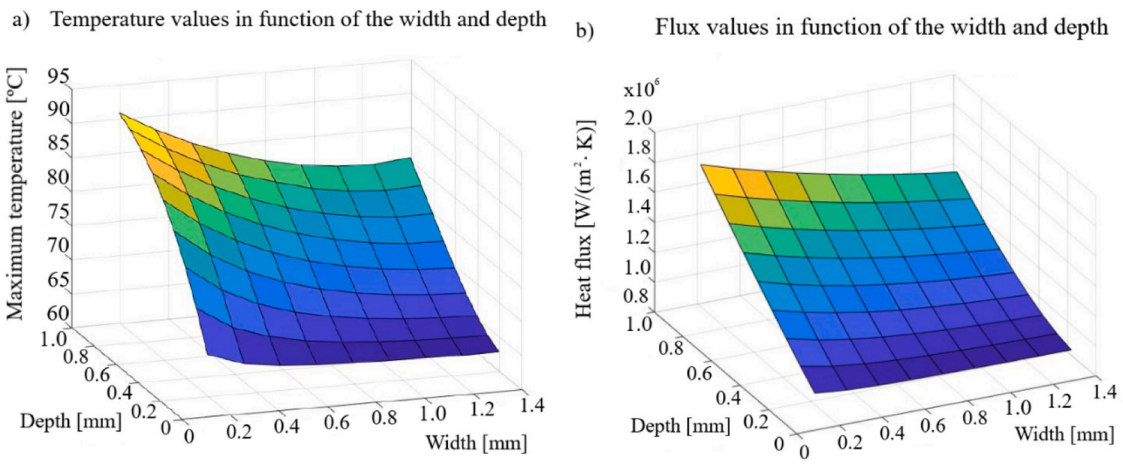

Fig. 7. - Parametric study results of a microchannel on a Cr_2AlC MAX phase plate for (a) maximum temperature; (b) heat flux (bottom surface).

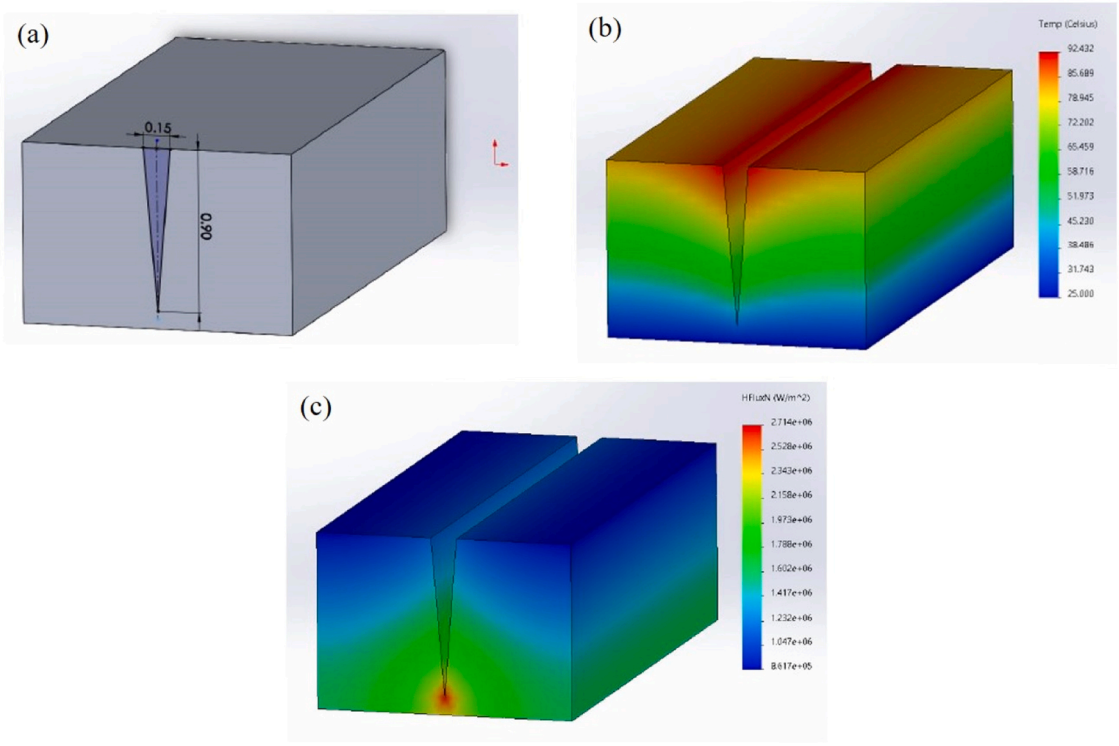

Fig. 8. - Temperature and heat flux result of the optimal geometry channel: (a) channel's dimensions, depth= 0.9 mm and width= 0.15 mm; (b) temperature behaviour; (c) heat flux behaviour through the plate in Cr_2AlC material.

thickness, which is relevant to understand its influence in thermal and heat flux simulation.

3.2. Numerical simulations results

3.2.1. Temperature analysis: theoretical vs. experimental results

This section compares the analytical and simulated results of the temperature analysis. Wet surface temperature, T_{wet}, was obtained by

$$q''_{convection} = q''_{conduction} \leftrightarrow h \cdot (T_{wet} - T_{\infty}) = -k \cdot \frac{T_{wet} - T_{in}}{e_{plate}} \quad (4)$$

Solidworks thermal analyses were performed to determine the wet surface temperature for stainless steel, Cr_2AlC and alumina plates. Fig. 4 shows the temperature variation through the thickness of a representative plate. Table 6 shows the analytical and numerical results for maximum wet temperature for the 316 L SS, Cr_2ALC and alumina plates, demonstrating the closest values in both methods for different materials.

Table 8
Ratio values of width and depth channels obtained from laser texturing.

	10 s			20 s		
22.5 W Air	0.53	0.51	0.48	0.39	0.45	0.4
25 W Air	0.6	0.49	0.48	0.46	0.44	**0.38**
25 W Argon	0.62	0.68	0.57	0.52	0.52	-

3.2.2. Convergence study

In a finite element simulation, generally the finer the mesh, the more accurate the values are. However, computation cost increases when

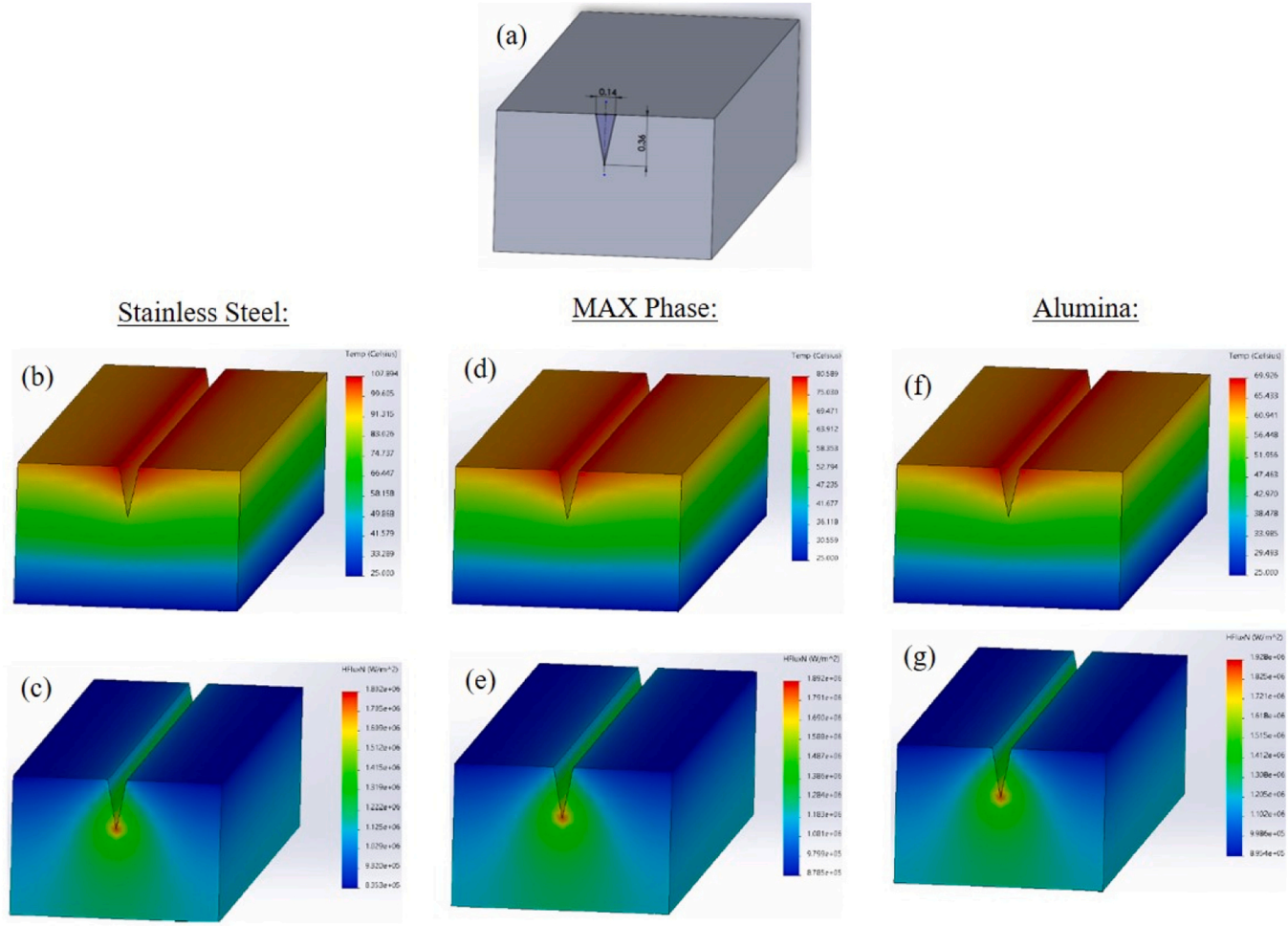

Fig. 9. - Simulation results of the optimised V-shape channel geometry textured with laser at air with a 25 W, 20 s: (a) channel geometry dimensions; (b) 316 L SS maximum temperature and (c) heat flux gradient; (d) Cr_2AlC maximum temperature and (e) heat flux gradient; (f) alumina maximum temperature; (g) heat flux gradient.

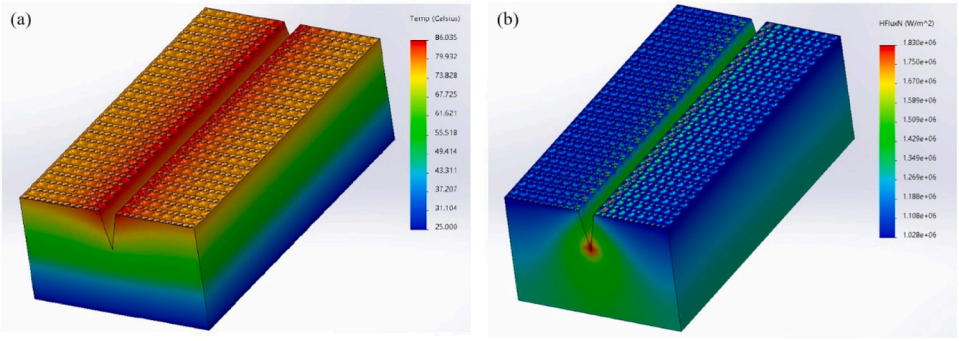

Fig. 10. - Simulation results of the Cr_2AlC corrugated plate and optimised geometry channel: (a) maximum temperature; (b) heat flux gradient.

reducing the mesh size, causing the simulation to take longer. An admissible mesh can be obtained by performing a convergence study, where the number of degrees of freedom is increased to obtain a reference value. The simulation values tend towards a specific number when the mesh gets finer. When the reference value's relative variation gets very small for duplication of degrees of freedom, usually 0.5%, an admissible mesh is obtained [38].

The convergence study was performed using a CAD model considering the channel size obtained for the optimised laser texturing condition and considering the Cr_2AlC MAX phase material properties. Table 7 presents the values obtained from the simulation of the finite element meshes shown in Fig. 5. The element size is the only input, starting with the coarsest mesh until reaching convergence.

A mesh can be considered admissible when the relative variation of the studied property is lower than 0.5% [38]. Although maximum temperature variations are not significant when element values increase, to obtain the admissible mesh, the maximum temperature and temperature's relative variation with the number of degrees of freedom is illustrated in Fig. 6.

Fig. 6. b shows that temperature's relative variation is lower than

0.1% for all the considered meshes. Thus, the chosen admissible mesh was the one with an element size of 0.1 mm and a tolerance of 0.05 mm since it combines a very low relative variation and a short computation time.

3.2.3. Parametric study

A parametric study was performed to obtain the optimal geometry of the microchannel, varying its width and depth, in a plate geometry of 1.5 mm width and 1 mm thickness. The channel optimisation was determined from the construction of channels where width varies for a certain percentage of the plate's width, and depth was similarly defined to a certain percentage of the thickness plate. The parametric study was performed from 10% to 90% in steps of 10% for width and thickness. The studied parameters were: i) maximum temperature of the plate; ii) temperature at the vertex of the groove; and iii) flux at the bottom surface of the plate, resulting in a total of 243 simulations on these three points of analysis. Fig. 7(a) and (b) show the parametric results for temperature and (bottom surface) heat flux behaviour in the simulation of the Cr_2AlC plate.

Maximum temperature and heat flux values were found for maximum depth and minimum width in a similar way as described by Yang et al. [40] in their size channels optimisation study to improve a printed circuit heat exchanger (PCHE), demonstrating that gradient temperature increases when the depth of the channels increases, and the width decreases. According to the results obtained in the parametric study, the optimal channel that maximises temperature and heat flux corresponds to the geometry with 10% ($1.5 \times 0.1 = 0.15$ mm) related to plate width; and 90% of the plate depth ($1 \times 0.9 = 0.9$ mm), as illustrated in Fig. 8.

The geometry channel presented above is the optimum inside the geometric limits proposed in this parametric study.

3.3. Laser texture and parametric results evaluation

This section analyses the best channel geometry obtained from laser texturing among the parametric results. Consequently, to compare Cr_2AlC laser texturing with the parametric results, width and depth sizes were converted into ratio values, as presented in Table 8, and related to optimal parametric results.

Since the best heat flux was found for the lowest width and highest depth, the best geometry respecting this relation was the one found for the lowest ratio value of 0.38, which corresponds to laser parameters of a 25 W power laser during 20 s exposure time, presenting 144 ± 5 μm width and 338 ± 16 μm depth. Therefore, the channel's depth should be increased compared to the optimal parametric results of 150 μm width and 900 μm depth, corresponding to a ratio value of 0.17. Here, laser texturing technology can also be optimised to increase the channel's depth by manipulating focus distance, shifting z-axis focus to a more profound surface level and repeating the laser pattern over the last laser passes.

Next, maximum temperature and heat flux numerical analysis will be performed considering laser texturing channel size of 144 μm width and 338 μm depth on the three materials, 316 L stainless steel, Cr_2AlC and alumina. Fig. 9 presents the numerical results of the optimal laser geometry for 316 L stainless steel, Cr_2AlC MAX phase and alumina.

The maximum heat flux results revealed that alumina has the higher value of $1.928 \times 10^6 W/m^2$ than the other materials. MAX phase has the second highest maximum heat flux, 1.892×10^6 W/m^2, and stainless steel has 1.802×10^6 W/m^2. The difference in heat flux for the MAX phase and alumina is 1.9%, and the stainless steel to the MAX phase is almost 5%. Regarding these differences, Cr_2AlC shows excellent heat transfer capacity, according to the literature [21,35].

3.4. Heat flux behaviour with corrugated surface

The complete laser texture was simulated in this section by integrating the corrugate surface section on the channel model. From the profilometry, the extracted corrugated section has a maximum height of ~40 μm (z_{max}), corresponding to the distance between the highest peak and deepest valley, with an angle of 60° between peaks and valleys. The distance between the top of the peaks is ~100 μm, and their diameter is ~20 μm. The corrugated part corresponds to 2.6% of the total plate thickness. Fig. 10 illustrates the values of the maximum temperature and heat flux of the combined texture composed of the corrugated surfaces with the optimised V-shape spaced channel for the Cr_2AlC MAX Phase.

The results obtained for the complete surface were 86.04 °C for the maximum temperature and $1.83 \times 10^6 W/m^2$ for the maximum flux on the vertex, and the bottom surface's heat flux was $1.34 \times 10^6 W/m^2$. Comparing this value with that of the Cr_2AlC plate without corrugation, cf. Fig. 9(e), which was 1.22×10^6 W/m^2, one observes that adding corrugation to the plate is an attractive solution to increase heat flux, which increased by 9.8% with the application of the corrugation.

4. Conclusions

The main objective of this study was to optimise the laser texturing of a Cr_2AlC MAX phase plate of a microplate heat exchanger and to study the influence of this study on the heat flux behaviour.

It was possible to perform complex textures, combining a corrugated surface with V-shaped spaced channels in a step of 300 μm, with ~340 μm depth, corresponding to 34% of the plate thickness.

Simulation results indicated that ceramics materials (alumina and MAX phase) presented better heat transfer behaviour, with alumina having the highest heat flux. The heat flux difference between Cr_2AlC and alumina (1.9%) is much lower when compared to 316 L stainless steel (4.8%), placing Cr_2AlC as a promising heat exchanger material.

The results obtained from the parametric study indicated that, for higher heat transfer, the optimal geometry channels are the minimum width and maximum depth. Based on laser surface texturing conditions, the optimal channels were found for 25 W at air and 20 s, presenting approximately 145 μm width and 340 μm depth.

Regarding the corrugated plate, the heat flux value is higher than the flat plate's. In analysis, the corrugated section, which corresponds to 2.6% of the plate's total thickness, has increased the heat flux by 9.8%. This increment in the heat flux was expected and therefore designed since the corrugation effect increases directly in heat conduction.

Declaration of Competing Interest

The authors declare that they have no known competing financial interests or personal relationships that could have appeared to influence the work reported in this paper.

Acknowledgements

This work had the financial support of the projects UIDB/00481/2020, UIDP/00481/2020, UIDB/50025/2020, UIDP/50025/2020 FCT – Fundação para Ciência e Tecnologia; and CENTRO-01-0145-FEDER-022083 - Centro Portugal Regional Operational Programme (Centro2020), under the PORTUGAL 2020 Partnership Agreement, through the European Regional Development Fund. This work is funded by national funds (OE), through FCT – Fundação para a Ciência e a Tecnologia, I.P., in the scope of the framework contract foreseen in the numbers 4, 5 and 6 of the article 23, of the Decree-Law 57/2016, of August 29, changed by Law 57/2017, of July 19. Also, the co-author R. M. S. Reis acknowledges JECS Trust under contract number 2021263.

References

[1] F. Wang, J.D. Harindintwali, Z. Yuan, M. Wang, F. Wang, S. Li, Z. Yin, L. Huang, Y. Fu, L. Li, S.X. Chang, L. Zhang, J. Rinklebe, Z. Yuan, Q. Zhu, L. Xiang, D.C. W. Tsang, L. Xu, X. Jiang, J. Liu, N. Wei, M. Kästner, Y. Zou, Y. Sik Ok, J. Shen, D. Peng, Wei Zhang, D. Barceló, Y. Zhou, Z. Bai, B. Li, B. Zhang, Ke Wei, Hujun Cao, Zhiliang Tan, Liu-bin Zhao, Xiao He, J. Zheng, Nanthi Bolan, Xiaohong Liu, C. Huang, S. Dietmann, Ming Luo, Nannan Sun, Jirui Gong, Yulie Gong, F. Brahushi, Tangtang Zhang, Cunde Xiao, Xianfeng Li, Wenfu Chen, Nianzhi Jiao, J. Lehmann, Yong-Guan Zhu, Hongguang Jin, Andreas Schäffer, James M. Tiedje, Jing M. Chen, Technologies and perspectives for achieving carbon neutrality, Cell Press, p. 100180, Nov. 28, Innovation vol. 2 (4) (2021), https://doi.org/10.1016/j.xinn.2021.100180.

[2] M. Fodstad, P.C. del Granado, L. Hellemo, B.R. Knudsen, P. Pisciella, A. Silvast, C. Bordin, S. Schmidt, J. Straus, Next frontiers in energy system modelling: a review on challenges and the state of the art, Renew. Sustain. Energy Rev. (2022), 112246, https://doi.org/10.1016/j.rser.2022.112246.

[3] K. Yuan, J. Shi, W. Aftab, M. Qin, A. Usman, F. Zhou, Y. Lv, S. Gao, R. Zou, Engineering the thermal conductivity of functional phase-change materials for heat energy conversion, storage, and utilisation, Adv. Funct. Mater. vol. 30 (8) (2020) 1904228, https://doi.org/10.1002/adfm.201904228.

[4] A.B. Gallo, J.R. Simões-Moreira, H.K.M. Costa, M.M. Santos, E. Moutinho dos Santos, Energy storage in the energy transition context: a technology review, in: Renewable and Sustainable Energy Reviews, vol. 65, Elsevier Ltd, 2016, pp. 800–822, https://doi.org/10.1016/j.rser.2016.07.028.

[5] C.J. Heard, J. Čejka, M. Opanasenko, P. Nachtigall, G. Centi, S. Perathoner, 2D oxide nanomaterials to address the energy transition and catalysis, Adv. Mater. vol. 31 (3) (2019) 1801712, https://doi.org/10.1002/adma.201801712.

[6] S. Lugo, O. García-Valladares, R. Best, J. Hernández, F. Hernández, Numerical simulation and experimental validation of an evacuated solar collector heating system with gas boiler backup for industrial process heating in warm climates, Renew. Energy vol. 139 (2019) 1120–1132, https://doi.org/10.1016/j.renene.2019.02.136.

[7] A. Hajatzadeh Pordanjani, S. Aghakhani, M. Afrand, B. Mahmoudi, O. Mahian, S. Wongwises, An updated review on application of nanofluids in heat exchangers for saving energy, in: Energy Conversion and Management, vol. 198, Elsevier Ltd, 2019, 111886, https://doi.org/10.1016/j.enconman.2019.111886.

[8] M. Shahabuddin, M.A. Alim, T. Alam, M. Mofijur, S.F. Ahmed, G. Perkins, A critical review on the development and challenges of concentrated solar power technologies (no. June), Sustain. Energy Technol. Assess. vol. 47 (2021), 101434, https://doi.org/10.1016/j.seta.2021.101434.

[9] H.L. Zhang, J. Baeyens, J. Degrève, G. Cacères, Concentrated solar power plants: review and design methodology, Renew. Sustain. Energy Rev. vol. 22 (2013) 466–481, https://doi.org/10.1016/j.rser.2013.01.032.

[10] R.P. Merchán, M.J. Santos, A. Medina, A. Calvo Hernández, High temperature central tower plants for concentrated solar power: 2021 overview, Renew. Sustain. Energy Rev. vol. 155 (2022), 111828, https://doi.org/10.1016/j.rser.2021.111828.

[11] X. Py, Y. Azoumah, R. Olives, Concentrated solar power: current technologies, major innovative issues and applicability to West African countries, Renew. Sustain. Energy Rev. vol. 18 (2013) 306–315, https://doi.org/10.1016/j.rser.2012.10.030.

[12] F. Sutter, C. Oskay, M.C. Galetz, T. Diamantino, F. Pedrosa, I. Figueira, S. Glumm, A. Bonk, A. Agüero, S. Rodríguez, T.J. Reche-Navarro, S. Caron, Dynamic corrosion testing of metals in solar salt for concentrated solar power, Sol. Energy Mater. Sol. Cells vol. 232 (no.) (2021), https://doi.org/10.1016/j.solmat.2021.111331.

[13] J.J.C.S. Santos, J.C.E. Palacio, A.M.M. Reyes, M. Carvalho, A.J.R. Freire, M. A. Barone, Concentrating solar power (December), in: Advances in Renewable Energies and Power Technologies, vol. 1, Elsevier, 2018, pp. 373–402, https://doi.org/10.1016/B978-0-12-812959-3.00012-5 (December).

[14] X. Zhang, H. Keramati, M. Arie, F. Singer, R. Tiwari, A. Shooshtari, M. Ohadi, Recent developments in high temperature heat exchangers: a review, Front. Heat. Mass Transf. vol. 11 (no) (, 2018), https://doi.org/10.5098/hmt.11.18.

[15] A. Sommers, Q. Wang, X. Han, C. T'Joen, Y. Park, A. Jacobi, Ceramics and ceramic matrix composites for heat exchangers in advanced thermal systems-a review, Appl. Therm. Eng. vol. 30 (11–12) (2010) 1277–1291, https://doi.org/10.1016/j.applthermaleng.2010.02.018.

[16] M. Caccia, M. Tabandeh-Khorshid, G. Itskos, A.R. Strayer, A.S. Caldwell, S. Pidaparti, S. Singnisai, A.D. Rohskopf, A.M. Schroeder, D. Jarrahbashi, T. Kang, S. Sahoo, N.R. Kadasala, A. Marquez-Rossy, M.H. Anderson, E. Lara-Curzio, D. Ranjan, A. Henry, K.H. Sandhage, Ceramic–metal composites for heat exchangers in concentrated solar power plants, Nature vol. 562 (7727) (2018) 406–409, https://doi.org/10.1038/s41586-018-0593-1.

[17] J. Gonzalez-Julian, Processing of MAX phases: from synthesis to applications, J. Am. Ceram. Soc. vol. 104 (2) (2021) 659–690, https://doi.org/10.1111/jace.17544.

[18] J. Wang and Y. Zhou, Recent progress in theoretical prediction, preparation, and characterisation of layered ternary transition-metal carbides, vol. 39. 2009. doi: 10.1146/annurev-matsci-082908–145340.

[19] W.K. Pang, I.M. Low, Understanding and improving the thermal stability of layered ternary carbides in ceramic matrix composites, Adv. Ceram. Matrix Compos. (2014) 340–368.

[20] G. Dongre, A. Rajurkar, A. Haria, A. Kulkarni, R. Raut, Thermal modelling for laser machining of SS316 L, inconel 718 and Ti6Al4V, J. Phys. Conf. Ser. vol. 2070 (1) (2021), 012226, https://doi.org/10.1088/1742-6596/2070/1/012226.

[21] J.D. Hettinger, S. Lofland, P. Finkel, T. Meehan, J. Palma, K. Harrell, S. Gupta, A. Ganguly, T. El-Raghy, M. Barsoum, Electrical transport, thermal transport, and elastic properties of M2AlC (M=Ti, Cr, Nb, and V), Phys. Rev. B Condens Matter Mater. Phys. vol. 72 (11) (2005) 2–7, https://doi.org/10.1103/PhysRevB.72.115120.

[22] F. Incorpera, D. Dewitt, T. Bergman, A. Lavine, Fundamentos de transferência de calor e de massa, Rio de Janeiro, LTC, Brasil, 2007.

[23] F.A.S. Mota, E.P. Carvalho, M.A.S.S. Ravagnani, Modeling and design of plate heat exchanger. Heat Transfer Studies and Applications, InTech, 2015, https://doi.org/10.5772/60885.

[24] C.A. Lewinsohn, M.A. Wilson, J.R. Fellows, H.S. Anderson, Fabrication and joining of ceramic compact heat exchangers for process integration, Int J. Appl. Ceram. Technol. vol. 9 (4) (2012) 700–711, https://doi.org/10.1111/j.1744-7402.2012.02788.x.

[25] Y. Hong, Jincheng Lei, Michael Heim, Yang Song, Lei Yuan, Shenglong Mu, R. K. Bordia, Hai Xiao, Jianhua Tong, Fei Peng, Fabricating ceramics with embedded microchannels using an integrated additive manufacturing and laser machining method, J. Am. Ceram. Soc. vol. 102 (3) (2019) 1071–1082, https://doi.org/10.1111/jace.15982.

[26] I. Etsion, State of the art in laser surface texturing, J. Tribol. vol. 127 (1) (2005) 248–253, https://doi.org/10.1115/1.1828070.

[27] L.M. Vilhena, M. Sedlaček, B. Podgornik, J. Vižintin, A. Babnik, J. Možina, Surface texturing by pulsed Nd:YAG laser, Tribol. Int vol. 42 (10) (2009) 1496–1504, https://doi.org/10.1016/j.triboint.2009.06.003.

[28] D. Du, Y.F. He, B. Sui, L.J. Xiong, H. Zhang, Laser texturing of rollers by pulsed Nd: YAG laser, J. Mater. Process Technol. vol. 161 (3) (2005) 456–461, https://doi.org/10.1016/j.jmatprotec.2004.07.083.

[29] J.M. Gurgel, F.C. Viana, J.M. Medeiros, M.G. Silva, J.C. Santos, Análise teórica da transferência de talor e massa em sistemas evaporativos usando modelos de merkel e de poppe, Rev. Principia - Divulg. Científica e Tecnológica do IFPB vol. 1 (2016), https://doi.org/10.18265/1517-03062015v1n32p51-64.

[30] P. Kurowski, *Engineering analysis with SOLIDWORKS simulation 2018*. Mission, Kansas City: Stephen Schroff, SDC publications, 2018.

[31] M. Bahiraei, A. Monavari, Thermohydraulic characteristics of a micro plate heat exchanger operated with nanofluid considering different nanoparticle shapes, Appl. Therm. Eng. vol. 179 (no) (2020), https://doi.org/10.1016/j.applthermaleng.2020.115621.

[32] B. Alm, R. Knitter, J. Haußelt, Development of a ceramic micro heat exchanger design, construction, and testing, Chem. Eng. Technol. vol. 28 (12) (2005) 1554–1560, https://doi.org/10.1002/ceat.200500253.

[33] N. García-Hernando, A. Acosta-Iborra, U. Ruiz-Rivas, M. Izquierdo, Experimental investigation of fluid flow and heat transfer in a single-phase liquid flow micro-heat exchanger, Int J. Heat. Mass Transf. vol. 52 (23–24) (2009) 5433–5446, https://doi.org/10.1016/j.ijheatmasstransfer.2009.06.034.

[34] W. Tian, P. Wang, G. Zhang, Y. Kan, Y. Li, D. Yan, Synthesis and thermal and electrical properties of bulk Cr2AlC, Scr. Mater. vol. 54 (5) (2006) 841–846, https://doi.org/10.1016/J.SCRIPTAMAT.2005.11.009.

[35] J. Gonzalez-Julian, S. Onrubia, M. Bram, O. Guillon, Effect of sintering method on the microstructure of pure Cr2AlC MAX phase ceramics, J. Ceram. Soc. Jpn. vol. 124 (4) (2016) 415–420, https://doi.org/10.2109/jcersj2.15263.

[36] T.M. Meißner, C. Oskay, A. Bonk, B. Grégoire, A. Donchev, A. Solimani, M. C. Galetz, Improving the corrosion resistance of ferritic-martensitic steels at 600 °C in molten solar salt via diffusion coatings, Aug. 2021, Sol. Energy Mater. Sol. Cells vol. 227 (no.) (2020), 111105, https://doi.org/10.1016/j.solmat.2021.111105.

[37] Urbano Uelligton Secundes, Olga de Castro Vilela, Naum Fraidenraich, and Elielza Moura de Souza Barbosa, "Use of molten salts in the heliothermal solar generation," in *VII Congresso Brasileiro de Energia Solar*, 2018. Accessed: Jan. 19, 2023. [Online]. Available: ⟨https://anaiscbens.emnuvens.com.br/cbens/article/view/423/423⟩.

[38] J.A. Oliveira, J. Pinho-da-Cruz, F. Teixeira-Dias, Asymptotic homogenisation in linear elasticity. Part II: finite element procedures and multiscale applications, Comput. Mater. Sci. vol. 45 (4) (2009) 1081–1096, https://doi.org/10.1016/j.commatsci.2009.01.027.

[39] C. Lewinsohn, High-efficiency, ceramic microchannel heat exchangers, Am. Ceram. Soc. Bull. vol. 95 (4) (2015) 26–31.

[40] Y. Yang, Hongzhi Li, Mingyu Yao, Yifan Zhang, Chun Zhang, Lei Zhang, Shuaishuai Wu, Optimising the size of a printed circuit heat exchanger by multi-objective genetic algorithm, October 2019, Appl. Therm. Eng. vol. 167 (no.) (2020), 114811, https://doi.org/10.1016/j.applthermaleng.2019.114811.